

Low-frequency western Pacific Ocean sea level and circulation changes due to the connectivity of the Philippine Archipelago

Wei Zhuang,¹ Bo Qiu,² and Yan Du¹

Received 26 August 2013; revised 18 November 2013; accepted 22 November 2013; published 11 December 2013.

[1] Interannual-to-decadal sea level and circulation changes associated with the oceanic connectivity around the Philippine Archipelago are studied using satellite altimeter sea surface height (SSH) data and a reduced gravity ocean model. SSHs in the tropical North Pacific, the Sulu Sea and the eastern South China Sea (ESCS) display very similar low-frequency oscillations that are highly correlated with El Niño and Southern Oscillation. Model experiments reveal that these variations are mainly forced by the low-frequency winds over the North Pacific tropical gyre and affected little by the winds over the marginal seas and the North Pacific subtropical gyre. The wind-driven baroclinic Rossby waves impinge on the eastern Philippine coast and excite coastal Kelvin waves, conveying the SSH signals through the Sibutu Passage-Mindoro Strait pathway into the Sulu Sea and the ESCS. Closures of the Luzon Strait, Karimata Strait, and ITF passages have little impacts on the low-frequency sea level changes in the Sulu Sea and the ESCS. The oceanic pathway west of the Philippine Archipelago modulates the western boundary current system in the tropical North Pacific. Opening of this pathway weakens the time-varying amplitudes of the North Equatorial Current bifurcation latitude and Kuroshio transport. Changes of the amplitudes can be explained by the conceptual framework of island rule that allows for baroclinic adjustment. Although it fails to capture the interannual changes in the strongly nonlinear Mindanao Current, the time-dependent island rule is nevertheless helpful in clarifying the role of the archipelago in regulating its multidecadal variations.

Citation: Zhuang, W., B. Qiu, and Y. Du (2013), Low-frequency western Pacific Ocean sea level and circulation changes due to the connectivity of the Philippine Archipelago, *J. Geophys. Res. Oceans*, 118, 6759–6773, doi:10.1002/2013JC009376.

1. Introduction

[2] The waters around the Philippine Archipelago are a region of complex geometry, with a number of straits and passages connecting marginal seas and the open Pacific Ocean (Figure 1a). To the north of the Luzon Island, the water exchanges between the South China Sea (SCS) and the western Pacific through the wide and deep Luzon Strait (sill depth of ~2200 m). To the south, there exist two large, semienclosed, marginal seas, the Sulu Sea and the Celebes Sea, and other smaller basins, including the Bohol Sea and the Sibuyan Sea (see Figure 1b). The Sulu Sea is connected to the SCS through the Mindoro Strait (sill depth of ~500 m) to the north, and to the Celebes Sea through the Sibutu Passage (~270 m) to the south. Other straits within the Philippine Archipelago are shallower and have relatively

weaker water exchanges [e.g., Han *et al.*, 2009]. The wind forcing in this region is subject to the monsoon system, with the northeasterly winds prevailing during boreal winter and the southwesterly winds dominating during boreal summer [Wyrski, 1961].

[3] In the northwestern Pacific, the upper ocean circulation, as indicated by the absolute mean sea surface topography in Figure 2a, is characterized by the tropical and subtropical gyres that share the westward flowing North Equatorial Current (NEC). After encountering the eastern Philippine coast, the NEC bifurcates into the northward flowing Kuroshio and the southward flowing Mindanao Current (MC) [e.g., Nitani, 1972; Toole *et al.*, 1990; Hu and Cui, 1991; Qiu and Lukas, 1996; Lukas *et al.*, 1996].

[4] While the mainstream of the Kuroshio leaps across the Luzon Strait and continues northward, a fraction of it enters the Luzon Strait and circulates cyclonically across the SCS basin. Recent studies demonstrate that this latter circulation, called the SCS throughflow (SCSTF), plays an important role in the mass, heat, and freshwater balance in the SCS [e.g., Qu *et al.*, 2005, 2006; Wang *et al.*, 2006a; Fang *et al.*, 2009]. After passing through the SCS basin, a branch of the SCSTF enters the Sulu Sea via the Mindoro Strait and continues southward to the Celebes Sea through the Sibutu Passage [Metzger and Hurlburt, 1996; Han *et al.*, 2009]. Although the majority of the shallow SCSTF waters flow through the Karimata Strait, the Mindoro

¹State Key Laboratory of Tropical Oceanography, South China Sea Institute of Oceanology, Chinese Academy of Sciences, Guangzhou, China.

²Department of Oceanography, University of Hawaii at Manoa, Honolulu, Hawaii, USA.

Corresponding author: W. Zhuang, State Key Laboratory of Tropical Oceanography, South China Sea Institute of Oceanology, 164 West Xingang Rd., Guangzhou 510301, China. (zhuang@scsio.ac.cn)

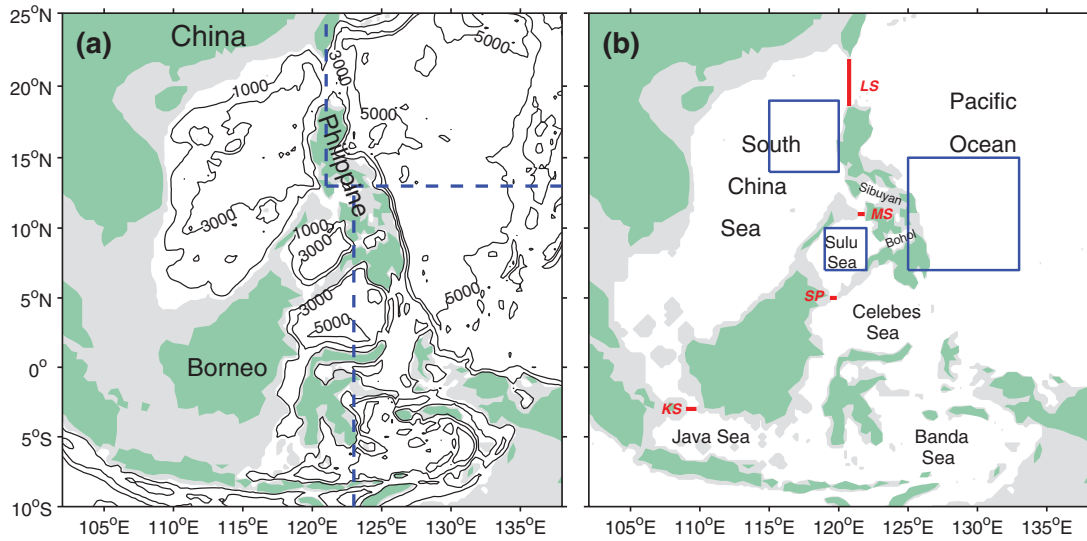


Figure 1. (a) Bottom topography of the tropical western Pacific and the adjacent marginal seas with the 1000, 3000, and 5000 m isobaths shown. Gray shading areas indicate the shelves shallower than 100 m, the model's boundary for Experiment 0. (b) The model geometry in Experiments 6 and 7, and the locations of Luzon Strait (LS), Mindoro Strait (MS), Sibutu Passage (SP), and Karimata Strait (KS). The three boxes are used for analyses of SSH anomalies representative for the western Pacific, the Sulu Sea, and the ESCS.

Strait-Sibutu Passage pathway is the only route for the SCSTF outflow at the thermocline depth [Qu and Song, 2009; Yaremchuk et al., 2009]. In addition, the Mindoro Strait-Sibutu Passage pathway contains most of the interannual-to-decadal signals of the SCSTF [Du and Qu, 2010; Gordon et al., 2012; Yu and Qu, 2013] and exerts a large impact on the mean circulation pattern in the north-western Pacific [Metzger and Hurlburt, 1996]. An enhanced mean transport through the Mindoro Strait, for example, can lead to a southward shift of the NEC bifurcation and a stronger Kuroshio transport.

[5] Dynamically, migration of the NEC bifurcation latitude (Y_b) is subject to the basin-scale wind forcing via baroclinic Rossby wave adjustment and displays a high correlation with the local sea level fluctuations [Qiu and Chen, 2010]. Accompanying the northward (southward) Y_b shift during El Niño (La Niña) years, the Kuroshio transport (KT) tends to decrease (increase) [Toole et al., 1990; Qiu and Lukas, 1996] and the Luzon Strait transport (LST) becomes stronger (weaker) [Qu et al., 2004]. Wu [2013] noted that the Y_b migration is also modulated by anomalous wind fluctuations off the Philippines that are related to the Pacific Decadal Oscillations (PDO).

[6] Several recent studies have noted that interannual sea level variations in the eastern SCS (ESCS) are highly correlated with the sea level signals near the eastern Philippine coast [Zheng et al., 2007; Liu et al., 2011; Wu, 2013]. The dynamic processes underlying the concurrent low-frequency sea level fluctuations around the Philippine Archipelago remain, however, controversial. Zheng et al. [2007] regarded the interannual sea level signals in the ESCS to be modulated by the westward Kuroshio intrusion along the northern coast of the Luzon Island. On the other hand, Liu et al. [2011] suggested that coastal Kelvin waves generated by the sea surface height (SSH) anomalies along

the east coast of the Philippines propagate through the Sibutu Passage and the Mindoro Strait and induce the inter-annual SSH variability in the ESCS. As the upper LST is determined by the meridional pressure gradient across the Luzon Strait, the sea level in the ESCS is dynamically important in serving as a good indicator for the interannual variability of the Kuroshio intrusion [Wu, 2013]. Aside from the possible influences via the oceanic connections,

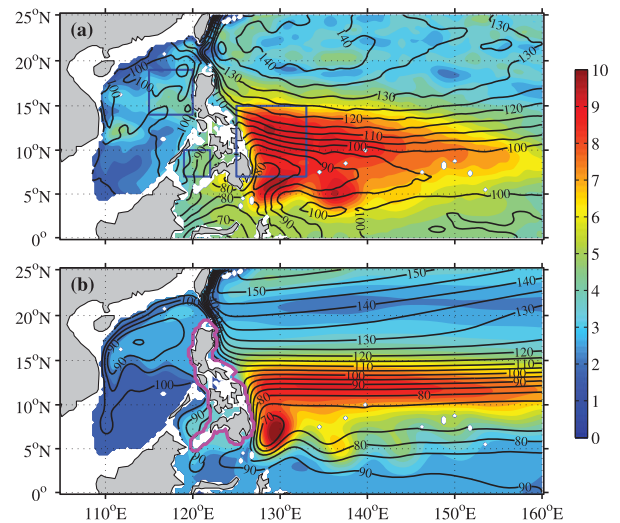


Figure 2. The standard deviation of sea level interannual-to-decadal variability (cm, shaded areas) and the mean SSH fields (cm, contours) for (a) altimeter observations, and (b) reduced-gravity model simulations. The boxes in Figure 2a are the same as those in Figure 1b. The pink line in Figure 2b shows the pathway of coastal waveguide around the Philippine Archipelago.

the SCS monsoon is highly correlated with the El Niño and Southern Oscillation (ENSO) [Fang *et al.*, 2006], due to the atmospheric teleconnection with the central Pacific linked by the anomalous lower-tropospheric anticyclones/cyclones in the western North Pacific [Wang *et al.*, 2000]. At present, effects of the local winds on the interannual sea level variability in the ESCS remain unclear.

[7] In order to better understand the sea level and circulation variability around the Philippine Archipelago, the present study aims to clarify the dynamics governing the correlated low-frequency SSH signals between the western Pacific and the ESCS by utilizing a nonlinear reduced gravity model. Throughout this study, the low-frequency variability is defined as the interannual-to-decadal signals with periods longer than 13 months. In addition, we will examine the impact of the SCSTF branch through the Mindoro Strait and the Sibutu Passage on the low-frequency changes of the western boundary current (WBC) in the North Pacific. By combining the numerical model results with the time-dependent island rule theory [Firing *et al.*, 1999], we attempt to assess the extent to which the Mindoro Strait-Sibutu Passage pathway modulates the western Pacific WBC changes.

[8] The organization of this paper is as follows: section 2 introduces the observational data and the numerical experiments based on a 1.5-layer nonlinear reduced-gravity model. Section 3 describes the low-frequency sea level variations around the Philippine Archipelago and explores their governing dynamical processes. In section 4, we investigate the possible influence of the Mindoro Strait-Sibutu Passage pathway on the circulation changes in the western North Pacific. Section 5 provides a summary and discussion.

2. Data and Model

2.1. Satellite Altimeter Data

[9] Satellite altimeter provides a near-global, high-resolution description of the variability in sea level and upper ocean circulations. In this study, we use a gridded sea level anomaly (SLA) data set from multisatellite altimeters, which are distributed by the Collecte Localisation Satellites (CLS) Space Oceanographic Division of Toulouse, France. To keep the sampling resolution of the total series homogeneous, we adopt the merged SLA data derived from simultaneous measurements of two satellites (Topex/Poseidon or Jason-1/2 + ERS or Envisat). The merged data set provides more realistic SLA and geostrophic velocity statistics than any individual data set [Ducret *et al.*, 2000]. Here we select the product with $1/4^\circ$ resolution, which is the same as the reduced-gravity model introduced below. Because the focus of the present study is on the low-frequency sea level variations, the original weekly data from October 1992 to December 2012 are temporally averaged to form a monthly SLA data set.

2.2. Mean Dynamic Topography

[10] To describe the large-scale circulation pattern and determine Y_b , the mean SSH field is required. Here we adopt a global $1/4^\circ$ resolution mean dynamic topography (MDT) produced by Rio *et al.* [2011], which combines the GRACE (Gravity Recovery and Climate Experiment)

geoid, surface drifting buoy measurements and hydrographic profiles. Compared to some other recent MDT estimates, this newly released MDT product is in better agreement with independent in situ observations [Rio *et al.*, 2011].

[11] As shown in Figure 2a, the observed MDT represents well the large-scale mean circulation features in the northwestern Pacific and the SCS. Due to the sparseness of the observational data, however, it is less capable of capturing the mesoscale flow patterns in some smaller basins (e.g., the Sulu Sea and the Celebes Sea) and through narrow straits.

2.3. The 1.5-Layer Nonlinear Reduced-Gravity Model

[12] In this paper, a 1.5-layer reduced-gravity model is used to investigate the low-frequency sea level and circulation variations associated with the pathway around the Philippine Archipelago. Previous studies have shown that the 1.5-layer reduced-gravity model contains essential dynamics in simulating the upper-ocean circulation in the Pacific and SCS [e.g., Metzger and Hurlbert, 1996; Wang *et al.*, 2006b; Chen and Wu, 2011]. The equations governing the upper-ocean motion in the 1.5-layer reduced-gravity system are:

$$\frac{\partial \mathbf{u}}{\partial t} + \zeta \mathbf{k} \times \mathbf{u} = -\nabla E + A_h \nabla^2 \mathbf{u} + \frac{\boldsymbol{\tau}}{\rho_0 h} - \frac{\varepsilon}{H} \mathbf{u} \quad (1)$$

$$\frac{\partial h}{\partial t} + \nabla \cdot (h\mathbf{u}) = 0 \quad (2)$$

where $\mathbf{u} = (u, v)$ is the horizontal velocity vector, $\boldsymbol{\tau}$ the surface wind stress vector, h the time-varying upper-ocean layer thickness, H the real-ocean bottom depth, ρ_0 the reference density, g' the reduced gravity, A_h the horizontal eddy viscosity coefficient, and ε the bottom friction coefficient. In equation 4, $\zeta = \mathbf{f} + \mathbf{k} \cdot \nabla \times \mathbf{u}$ denotes the absolute vorticity, and $E = g'h + (u^2 + v^2)/2$ is the total energy. In this 1.5-layer reduced-gravity model, SSH is given by $SSH = \frac{g}{g'} h$, where g is the gravitational constant.

[13] For the model's control run (Experiment 0), we set the model domain to be 30°S – 40°N and 100°E – 70°W , covering the tropical and subtropical Pacific and the eastern Asia marginal seas. Along the closed open ocean boundaries, no-slip boundary conditions are applied. Given that the signals generated in the tropical Pacific dominate the low-frequency variability around the Indonesian Archipelago [e.g., Meyers, 1996; Feng *et al.*, 2004; Wijffels and Meyers, 2004], Experiment 0 excludes the presence of the Indian Ocean (IO) and focuses on the variability in the western Pacific and the adjacent marginal seas. Possible impacts of the IO will be investigated later in this study through a model sensitivity experiment.

[14] The horizontal resolution of the model is $1/4^\circ \times 1/4^\circ$. It is initialized with a uniform upper layer thickness of 250 m and has parameter values $g' = 0.036 \text{ m s}^{-2}$, $A_h = 1200 \text{ m}^2 \text{ s}^{-1}$, and $\varepsilon = 15 \text{ m day}^{-1}$. Given that coastal Kelvin wave signals are able to transmit through the straits shallower than the thermocline, the 100 m isobath is defined as the land/sea boundary in Experiment 0 and a depth-dependent bottom friction ε/H is applied in the model to adjust the flow with topographic effect. The

Table 1. Numerical Experiments of the 1.5-Layer Reduced-Gravity Model

Model Experiments	Descriptions
Experiment 0	Control run, model domain 30°S–40°N and 100°E–70°W; closed lateral boundaries; original monthly ORA-S3 wind forcing; open the Luzon Strait, Mindoro Strait and Sibutu Passage, close the Karimata Strait
Experiment 1	The same geometry as Experiment 0. Original monthly wind over the SCS and the Sulu Sea; monthly climatological wind over the Pacific Ocean
Experiment 2	The same geometry as Experiment 0. Original monthly wind over the north Pacific (north of 13°N); monthly climatological wind over other regions
Experiment 3	The same geometry as Experiment 0. Original monthly wind over the south Pacific (south of 13°N); monthly climatological wind over other regions
Experiment 4	Close the Sibutu Passage; other configurations are the same as Experiment 0
Experiment 5	Close the Luzon Strait; other configurations are the same as Experiment 0
Experiment 6	Larger model domain (60°S–40°N, 30°E–70°W); original monthly ORA-S3 wind forcing, but decrease southward to 0 from 30°S to 40°S, to reduce strong outcropping at high latitude; open the Luzon Strait, Mindoro Strait, Sibutu Passage, Karimata Strait and ITF passages
Experiment 7	Similar to Experiment 6, but close the Sibutu Passage

Sibutu Passage and the Mindoro Strait are both $1/2^\circ$ wide in Experiment 0, slightly larger than their real widths (~ 30 km) at 100 m depth [e.g., *Gordon et al.*, 2011; *Sprintall et al.*, 2012]. Such coastline geometry excludes most of the shallow shelves and islands, but allows coastal Kelvin waves to pass through the Sibutu Passage and Mindoro Strait. With the first-mode baroclinic Rossby radii of deformation [*Chelton et al.*, 1998] estimated at ~ 90 km near the Mindoro Strait and ~ 200 km near the Sibutu Passage, the transmission of coastal Kelvin waves should be quite efficient, even approaching 100% for the low-frequency waves, according to previous theoretical and numerical model studies [*Qiu et al.*, 1999; *Durland and Qiu*, 2003; *Johnson and Garrett*, 2006]. Near the northern ($36^\circ\text{--}40^\circ\text{N}$) and southern ($26^\circ\text{--}30^\circ\text{S}$) boundaries of the model, A_h is increased linearly from 1200 to $6000\text{ m}^2\text{ s}^{-1}$ for the purpose of suppressing instabilities and outcropping in midlatitude regions.

[15] The surface wind forcing is derived from the monthly $1^\circ \times 1^\circ$ wind stress data from the European Center for Medium-Range Weather Forecast (ECMWF) Ocean Analysis System ORA-S3 [*Balmaseda et al.*, 2008]. This wind data set is based on ERA-40 and ERA Operational System wind stresses, but has been revised to reduce the perceived uncertainties in these two products. The model is first spun up from rest by the climatological monthly winds for 20 years. Then, a hindcast integration from 1959 to 2009 is conducted and the monthly averaged results are saved for analysis. As it takes less than 10 years for the baroclinic Rossby wave adjustments in the low-latitude region, we confine our analysis of the model results below to the period of 1970–2009.

[16] As shown in Figure 2b, the mean geostrophic circulation in Experiment 0 as represented by the mean SSH

generally reproduces the observational pattern. Both the observed and simulated circulation systems in the western Pacific show the westward flowing NEC, which bifurcates into the northward flowing Kuroshio and southward flowing MC as it reaches the eastern Philippine coast. In the SCS, both the observed and modeled mean SSH fields indicate a cyclonic circulation located mainly in the northern basin. As the model only captures the wind-driven component of the circulation, the simulated flow east of the Luzon Strait is westward. It fails to reproduce the observed eastward flowing Subtropical Countercurrent (STCC), whose appearance requires thermodynamic processes absent in the reduced-gravity model [e.g., *Cushman-Roisin*, 1984; *Kubokawa*, 1997; *Kobashi et al.*, 2006; *Kobashi and Kubokawa*, 2012], and its associated mesoscale eddy signals along the $18^\circ\text{--}25^\circ\text{N}$ band [*Qiu*, 1999]. This unrealistic westward flow east of the Luzon Strait leads to a stronger westward flow intrusion into the SCS and a relatively high LST of 6.3 Sv compared with the observations that range from 3 to 6.5 Sv [*Chu and Li*, 2000; *Qu et al.*, 2000; *Liang et al.*, 2003; *Tian et al.*, 2006; *Yaremchuk and Qu*, 2004].

[17] Also shown in Figures 2a and 2b are the standard deviations of the low-frequency SSH signals derived from altimetric observations and Experiment 0. To obtain the low-frequency signals, we first remove the dominant seasonal variations by subtracting the monthly climatological mean values; a 13-point Hanning filter is then applied to remove variations with periods shorter than 13 months. Both the observation and simulation reveal that the low-frequency SSH variability is strong in the tropical western Pacific between 5°N and 15°N and becomes weaker near the subtropical gyre and the equator. The low-frequency variance also reduces toward the Sulu Sea and northern SCS, and reaches its minimum in the southern SCS basin. In these marginal seas, the model shows weaker low-frequency SSH amplitude than the observations, probably due to the complex topography. Another possible cause is that the simulation of circulation changes in the marginal seas is sensitive to the choice of wind forcing [*Metzger*, 2003; *Zhuang et al.*, 2010]. More detailed model-data comparisons will be discussed later.

[18] In addition to Experiment 0, seven model sensitivity experiments are performed in order to further clarify the dynamical processes related to the pathway around the Philippine Archipelago. The configurations of these experiments are listed in Table 1 and will be described in the relevant sections.

3. Dynamics of Sea Level Changes Around the Philippine Archipelago

3.1. Sea Level Variations

[19] As noted in several previous studies, the interannual variability of SSH in the ESCS is well correlated with that in the tropical western Pacific [e.g., *Zheng et al.*, 2007; *Liu et al.*, 2011]. Figures 3a–3c show the low-frequency altimeter-derived SLAs (black lines) averaged in the tropical western Pacific, the Sulu Sea, and the ESCS; see the three boxes in Figures 1b and 2a for their locations. As shown in Figure 2a, these boxes are selected from the areas with enhanced low-frequency SSH variations. For a more direct comparison with the reduced-gravity model that does not

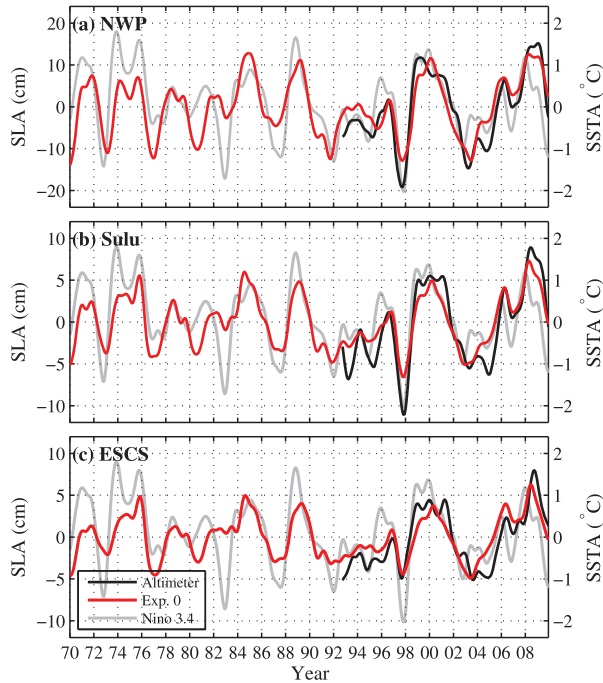


Figure 3. The SLAs time series derived from altimeter observation (black lines) and reduced-gravity model Experiment 0 (red lines), and the negative Nino-3.4 SSTA time series (gray lines). The SLAs are averaged within three boxes (shown in Figures 1b and 2a) in (a) the tropical northwestern Pacific, (b) the Sulu Sea, and (c) the ESCS.

include the sea level rise due to the thermal expansion under a warming climate and the freshwater input from land-ice melting, we subtract the 3.2 mm/yr global mean sea level rise trend [Willis *et al.*, 2010] from the observations. Visually, the observed SLAs in these three regions display very similar low-frequency variability. The signals in the western Pacific are correlated at 0.95 and 0.88 with those in the Sulu Sea and the ESCS, respectively. Note that the interannual-to-decadal SLA signals have greater amplitudes (defined as the standard deviations) in the western Pacific (8.3 cm) than in the Sulu Sea (4.8 cm) and the ESCS (3.4 cm), indicating possible dissipation and weakening of the signals during their transmission from the western Pacific into the marginal seas.

[20] Figure 3 shows that the SLAs from Experiment 0 (red lines) reproduce the observed low-frequency SLA signals favorably in all three boxes. For 1993–2009, the correlation coefficients between the observations and Experiment 0 reach 0.91, 0.92, and 0.82 in the western Pacific, the Sulu Sea and the ESCS, respectively. In addition, the low-frequency sea level variations show strong oscillations relating to the occurrence of the ENSO events (e.g., 1972/1973, 1987/1988, and 1997/1998) and a good correspondence between the negative Nino-3.4 index and the SLAs is easily discernible in Figure 3 (cf. red and gray lines). Over the period of 1970–2009 when the negative Nino-3.4 index leads the SLAs in Experiment 0 by about 2 months, their correlations reach the maxima of 0.67, 0.77, and 0.68 in the northwestern Pacific, the Sulu Sea, and the SCS, respectively.

3.2. Effects of Regional Wind Forcing

[21] Several previous studies have noted the close correlations between the ENSO and interannual variability of surface winds over the SCS [Wang *et al.*, 2000; Fang *et al.*, 2006]. With the straits around the Philippine Archipelago providing oceanic connections for possibly conveying the ENSO signals into the SCS [e.g., Qu *et al.*, 2004; Liu *et al.*, 2011], it is necessary to explore the relative roles played by the remote Pacific versus local winds in generating the low-frequency SSH changes in the marginal seas. To answer this question, we divide the model domain to three segments (see the dashed lines in Figure 1a): segment 1 includes the SCS, the Sulu Sea and the eastern IO; segment 2 occupies the open subtropical Pacific Ocean north of 13°N; segment 3 covers the open tropical Pacific Ocean south of 13°N. Three model experiments are designed to assess the importance of the wind forcing over different segments. In the sensitivity Experiment 1, we keep the interannually varying winds in segment 1, but use the climatological monthly winds in the Pacific Ocean. Similarly, in Experiments 2 and 3, the winds in segments 2 and 3 are interannually varying, respectively, while those outside the corresponding segment are the climatological monthly fields without low-frequency signals. In all these experiments, the modified winds are smoothed along the segment boundaries to eliminate sharp discontinuities.

[22] As shown in Figure 4, the sea level variations of Experiment 0 are generally tracked by Experiment 3 in all three boxes in Figure 1b, revealing the dominance of

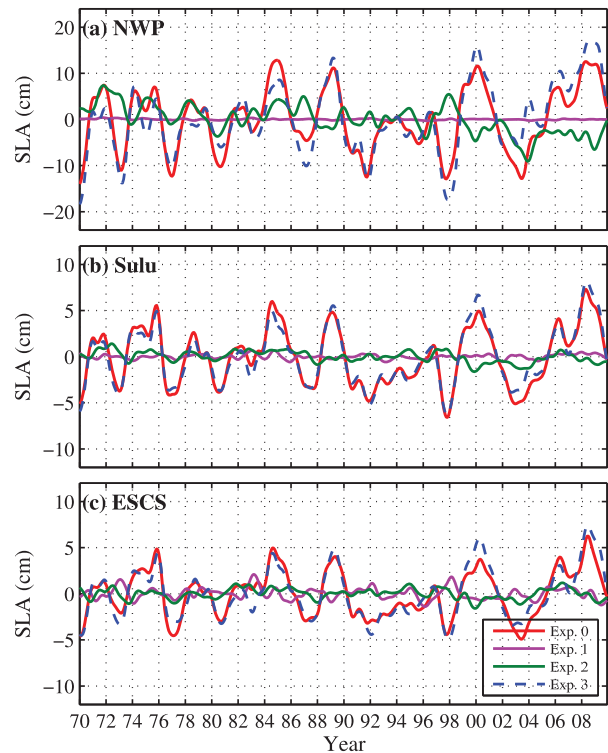


Figure 4. The SLAs time series derived from the model Experiments 0, 1, 2, and 3. The SLAs are averaged within three boxes (shown in Figures 1b and 2a) in (a) the tropical northwestern Pacific, (b) the Sulu Sea, and (c) the ESCS. The configurations of experiments are listed in Table 1.

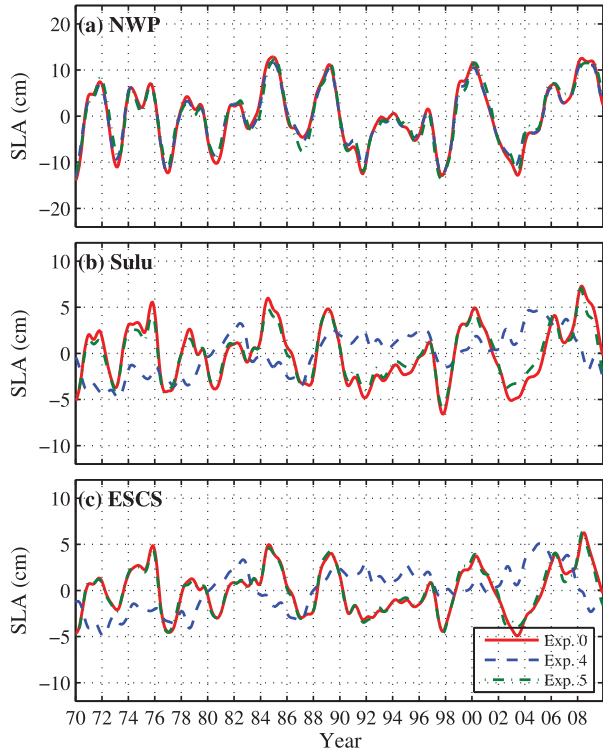


Figure 5. The same as Figure 4, but for the results of Experiments 0, 4, and 5.

tropical Pacific wind forcing to the low-frequency sea level changes around the Philippine Archipelago. To quantify the contributions of the wind forcing from different segments, we define the explained variances as $S = 1 - \langle (h_i - h_0)^2 \rangle / \langle h_0^2 \rangle$, where h_0 is the SLA time series in Experiment 0, h_i represents the result from Experiment i ($i = 1, 2$, or 3), and $\langle \rangle$ denotes the summation over time. In the western Pacific box (Figure 4a), the explained variances of Experiments 1–3 are 0.1%, –24%, and 75%, respectively, indicating that the SSH variability east of the Philippine coast is not affected by the winds to the west, but is caused by westward propagating Rossby waves forced by the basin-scale wind stress curls (WSC) in the Pacific [e.g., Qiu and Lukas, 1996; Qiu and Chen, 2012].

[23] In the Sulu Sea and the ESCS (Figures 4b and 4c), Experiment 3 explains 94.9% and 85.9% of the variance of Experiment 0, indicating that the low-frequency SSH variations within the marginal seas are mainly induced by the tropical Pacific wind forcing instead of the local or subtropical Pacific winds. Comparisons of Experiments 0–3 elucidate that it is the tropical ocean dynamics, rather than the atmospheric teleconnected wind forcing, that controls the low-frequency sea level signals in the Sulu Sea and the ESCS.

3.3. Importance of Coastal Kelvin Waves

[24] To investigate which channel is responsible for conveying the wind-driven SSH variability from the tropical western Pacific into the marginal seas, we conduct two more sensitivity experiments, one with the Sibutu Passage closed (Experiment 4) and the other with the Luzon Strait closed (Experiment 5). All other parameters and forcing

are kept the same in these two experiments as in Experiment 0.

[25] For the period of 1970–2009, the SLAs in Experiments 0, 4, and 5 display similar interannual-to-decadal variations near the eastern Philippine coast (Figure 5a), confirming the dominant effect of the tropical Pacific wind forcing as shown in Figure 4. However, large differences between Experiments 0 and 4 are found in the Sulu Sea and the ESCS (Figures 5b and 5c). With the closure of the Sibutu Passage, the low-frequency SSH signals in the Sulu Sea and the ESCS become much weaker in amplitude and are poorly correlated with those in the western Pacific. The correlation coefficients between the SSH time series from the altimetric observations and Experiment 4 drop to –0.26 for the Sulu Sea, and –0.51 for the ESCS. In contrast, the SLAs in Experiment 5 are almost identical to those in Experiment 0 (Figures 5b and 5c), suggesting that the closure of the Luzon Strait has little impact on the low-frequency sea level changes in the Sulu Sea and the ESCS.

[26] The results from Experiments 4 and 5 indicate that it is the Sibutu Passage rather than the Luzon Strait that controls the transmission of interannual-to-decadal sea level signals from the western Pacific into the Sulu Sea and the ESCS. Dynamically, SSH variations in the Sulu Sea and the ESCS are likely induced by coastal Kelvin waves propagating through the Sibutu Passage and the Mindoro Strait. To verify the roles of the coastal Kelvin waves around the Philippine Archipelago, we select a pathway delineated by the pink line in Figure 2b, along which the lag correlation of the modeled low-frequency SSH signals is calculated. The pathway starts at 124.5°E, 13°N near the NEC bifurcation Y_b , and circles the Archipelago clockwise. The SSH signals at 122°E, 8.5°N in the middle of Sulu Sea are taken as the reference time series.

[27] To the southeast of the Philippine Archipelago (with the distance between 0 and 1000 km in Figure 6a), the SSH variability largely results from the Rossby waves induced by the WSC forcing in the low-latitude North Pacific Ocean. Due to the slower long Rossby wave speed toward higher latitudes, the coastal sea level changes exhibit high correlation with time lags toward the higher latitude (Figure 6).

[28] After reaching the eastern coast of Philippine Archipelago, the low-frequency wave signals in Experiment 0 display pronounced along-coast propagations from the southeastern Mindanao Island toward the ESCS through the Sibutu Passage and the Mindoro Strait. As denoted by the green line in Figure 6a, the mean speed of these waves is ~ 2.3 m/s, consistent with the phase speed of the coastal Kelvin waves. The high-correlation band decreases abruptly near the Mindoro Strait, probably due to the alteration of sea level signals by the strong current through the strait. Similar interruptions happen southeast of the Mindanao Island and near the Luzon Strait, associated possibly with the recirculation of the Mindanao Current and the strong Kuroshio current, respectively (see Figure 2b). In Experiment 5, there is no SCSTF through the Mindoro Strait owing to the closure of the Luzon Strait, and the interruption of high-correlation band at the Mindoro Strait disappears (Figure 6b). The wave speed in Experiment 5 is largely the same as that in Experiment 0. The delayed increased correlation near the Mindoro Strait and the

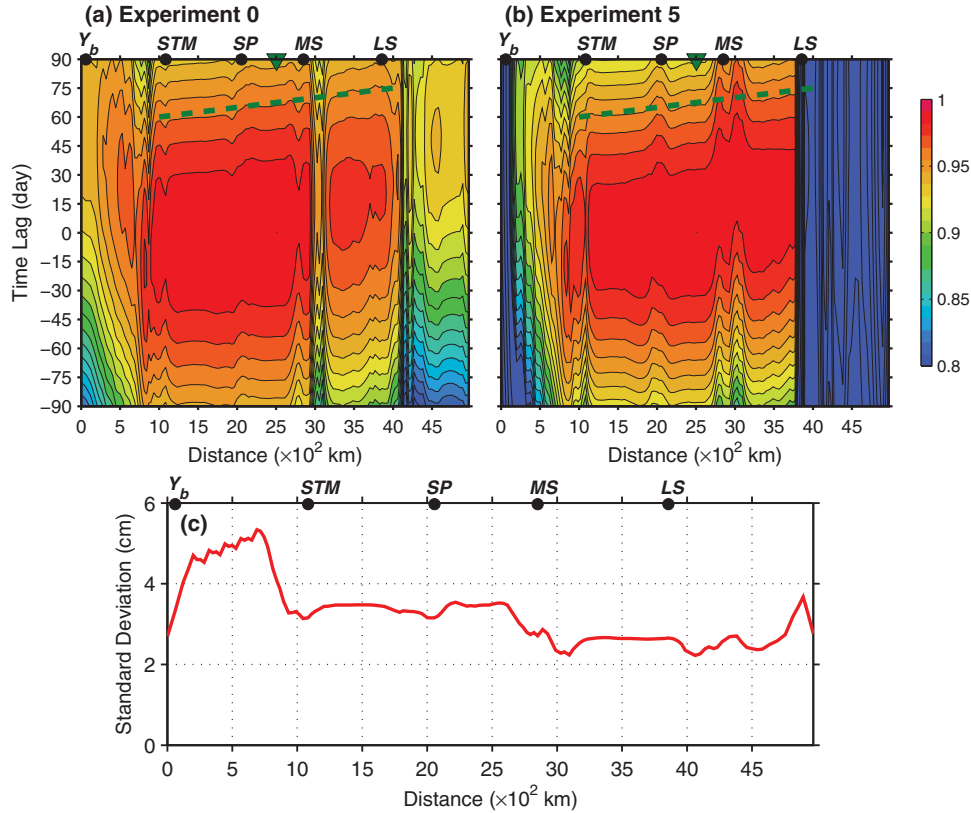


Figure 6. Time-distance lag correlations of the modeled low-frequency SSH along the coastal Kelvin Wave pathway around the Philippine Archipelago (see Figure 2b): (a) Experiment 0 and (b) Experiment 5. The SSHs in the middle of Sulu Sea (122°E , 8.5°N , the green triangles) are taken as the reference time series. The SP, MS, LS, and STM represent the positions of Sibutu Passage, Mindoro Strait, Luzon Strait, and the southern tip of Mindanao Island, respectively. (c) Standard deviations of the low-frequency SSH in Experiment 0 along the coastal Kelvin Wave pathway around the Philippine Archipelago.

Sibutu Passage in Figure 6b is likely due to the closure of the Luzon Strait, which allows the coastal Kelvin waves to circulate within both the SCS and the Sulu Sea.

[29] Along the Kelvin wave's pathway, the model results show comparable amplitudes of the low-frequency SSH variability to the south of Mindanao Island, along the eastern Sulu Sea and along the eastern SCS (Figure 6c), indicating the efficient transmission of Kelvin wave energy through the Sibutu Passage and the Mindoro Strait. *Durand and Qiu* [2003] found that, under the linear and inviscid dynamics assumption, an arbitrarily narrow strait can transmit virtually all of the Kelvin wave energy at the low-frequency limit. They also noted that the wave energy can almost totally transmit through the Lombok Strait, whose minimum width is about 0.2 times the local first-mode baroclinic Rossby radius (similar to the Sibutu Passage and the Mindoro Strait). More accurate quantification of energy transmission through the straits within the Philippine Archipelago will, however, require considerations of complex bathymetry, nonlinear advection, and eddy dissipation, which are beyond the scope of our present study.

[30] Along the eastern boundary of the SCS, the coastally trapped Kelvin waves can radiate westward propagating Rossby waves, contributing to the circulation adjustment in the interior SCS. The numerical results

shown in Figure 6c reveal, however, that the energy loss from the coastal Kelvin waves to Rossby waves is relatively weak. This is likely due to the short meridional distance, $\sim 5^\circ$ latitude, the Kelvin waves have to travel from the Mindoro Strait to the northern tip of Luzon Island.

3.4. Possible Impacts From the IO and ITF

[31] In Experiments 0–5, we have assumed that the IO and ITF exert little impact around the Philippine Archipelago and have closed the model's southwestern boundary along the eastern IO. To examine the possible impact from the IO and ITF, we extend the model domain to 60°S – 40°N , 30°E – 70°W in Experiment 6. Experiment 6 is also driven by the monthly ECMWF ORA-S3 winds. To avoid strong outcropping at high latitudes, the wind stresses are gradually reduced southward from 100% at 30°S to 0 south of 40°S . As the ITF is driven by the large-scale wind in the Pacific [Godfrey, 1989], elimination of the wind forcing at high latitudes results in a lower ITF transport value of 5.1 Sv. In Experiment 6, both the Karimata Strait and the Java Sea are open and defined by the 20 m isobaths. The inflow through the Luzon Strait in Experiment 6 (6.5 Sv) is close to that in Experiment 0 and is balanced by the outflow from the Mindoro (3.2 Sv) and Karimata (3.3 Sv) Straits. To check the possibility of wave transmissions through the

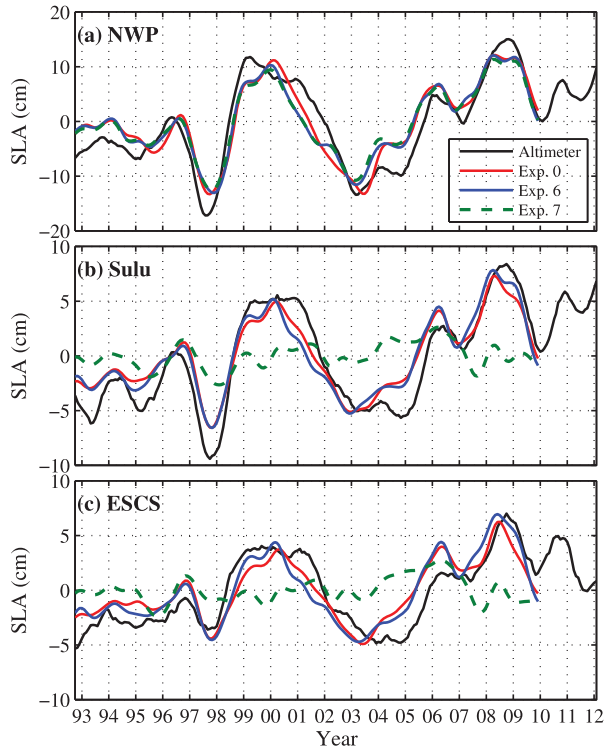


Figure 7. The same as Figure 4, but for the SLAs time series from altimeter observations, Experiments 0, 6, and 7 during the 1993–2012 period.

Karimata Strait into the ESCS, we also run Experiment 7, which is the same as Experiment 6 but with the Sibutu Passage closed. In this case, the LST is reduced to 4 Sv likely due to the strong depth-dependent bottom friction in the Karimata Strait and the Java Sea.

[32] In Experiment 6, variability of the Sibutu Passage inflow into the Celebes Sea is ENSO-sensitive and out-of-phase with the Mindanao Current inflow into the Celebes Sea (not shown). This result resembles the three-dimensional model simulation in *Gordon et al.* [2012] and suggests the effect of SCSTF's modulation on the ITF inflow. The variability of ITF through the main outflow passages (Lombok Strait, Ombai Strait, and Timor Passage), however, remains unchanged between Experiments 6 and 7, confirming that the circulation through the Luzon Strait-Sibutu Passage pathway changes the variability amplitude of the ITF inflow into the Celebes Sea [*Gordon et al.*, 2012], but has little impact on the total ITF outflow into the IO [*Metzger and Hurlbert*, 1996].

[33] Figures 7a–7c compare the low-frequency SLAs around the Philippine Archipelago derived from altimeter observations, Experiments 0, 6, and 7. The observed sea level signals in all three boxes are well captured by both Experiments 0 and 6. The negligible difference between Experiments 0 and 6 suggests that the IO signals do not significantly alter the sea level variations around the Philippine Archipelago via the ITF passages. Similar to Experiment 4, closure of the Sibutu Passage in Experiment 7 does not affect the sea level variability in the western Pacific but leads to significant weakening of sea level amplitudes in the Sulu Sea and the ESCS. The above

results indicate that the SLA signals in the open ocean can only transmit into the Sulu Sea and the ESCS via the Sibutu Passage-Mindoro Strait pathway. Opening of the ITF passages and the Karimata Strait imparts little influence upon this process.

4. Regional Low-Frequency Circulation Changes

[34] Experiments with the open versus closed Sibutu Passage (Experiment 0 minus Experiment 4) indicate that the existence of the SCSTF branch through the Sibutu Passage results in an anomalous circulation pattern with the cyclonic circulation over the northern SCS basin and the northward flow along the eastern Philippine coast (Figure 8). The difference between opening and closure of the Luzon Strait (Experiment 0 minus Experiment 5) produces the same anomalous flow pattern as Figure 8. Presence of the anomalous northward flow along the eastern Philippine coast implies a southward shift of Y_b , a stronger KT and a weaker Mindanao Current transport (MCT), consistent with the results of *Metzger and Hurlbert* [1996]. In this section, we will further investigate the effects of the pathway around the Philippine Archipelago to the low-frequency variations of Y_b , KT, and MCT.

4.1. The Variability of Y_b

[35] Y_b denotes the crossroad of subtropical and tropical gyres and is important in determining the meridional heat and water mass exchanges between the North Pacific tropical and subtropical gyres [*Fine et al.*, 1994]. In both the observations and model simulations, the Y_b value can be found at where the meridional geostrophic flow is zero within the 2° band along the Philippine coast [*Qiu and Chen*, 2010]. In the case of multiple zero crossings, we select the Y_b point where the SSH value can be traced upstream to the core of the westward flowing NEC.

[36] The Y_b time series derived from Experiments 0 to 4 generally capture the phase of altimeter-derived low-frequency Y_b variability with correlation coefficients of 0.76 and 0.72, respectively (Figure 9a). However, as shown in Figure 9a, the modeled Y_b time series in both runs are more northward and weaker in amplitude than the observations. This is because the altimeter data represent the geostrophic velocity at the sea surface, whereas the modeled results represent the upper-layer averaged geostrophic flow. Y_b has a tendency to shift poleward with increasing depth [*Qu and Lukas*, 2003].

[37] The mean Y_b in Experiment 0 is 13.7°N . With the closure of the Sibutu Passage, the mean Y_b moves northward to 14.5°N . The northward shift of Y_b is consistent with the anomalous circulation pattern in Figure 8. As shown in Figure 9a, the Y_b values in Experiment 4 are always north of those in Experiment 0 during the 1970–2009 period. The low-frequency Y_b signals in these two runs show very similar temporal variations with a correlation coefficient of 0.91. This is consistent with the previous findings that Y_b is determined by the wind-driven Rossby wave adjustment in the Pacific basin [e.g., *Qiu and Chen*, 2010]. A closer inspection of their standard deviations, however, reveals that the Y_b amplitude in Experiment 0 (0.50°) is about 18% lower than that in Experiment 4 (0.61°), suggesting weakening of the Y_b variability due to

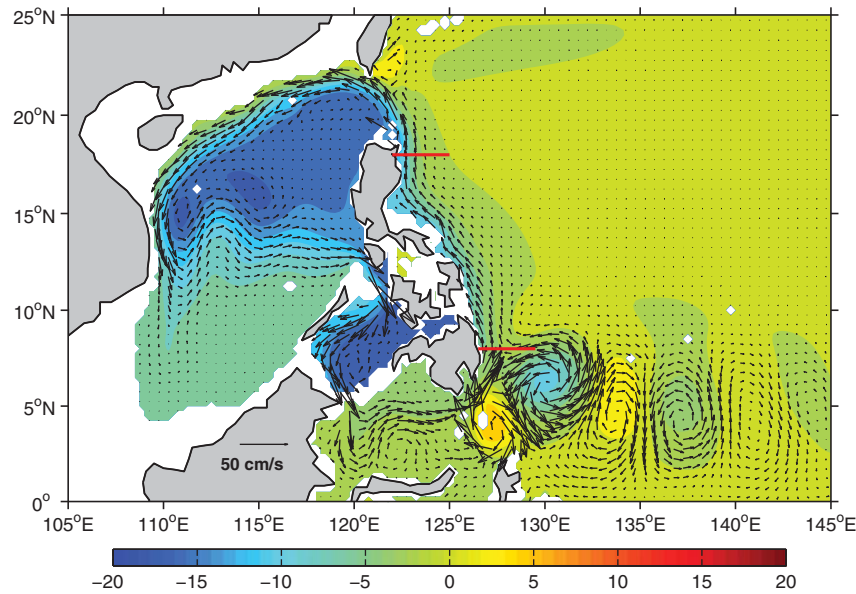


Figure 8. Mean SSH and currents anomalies from Experiment 0 minus Experiment 4. The red lines denote the transects for KT and MCT estimations at 18°N and 8°N, respectively.

the oceanic pathway west of the Philippine Archipelago. On the decadal time scales, both the observations and simulations show southward migration trends of Y_b during the satellite altimeter era of 1993–2009. Prior to the 1990s, the simulated Y_b time series exhibit weaker northward trends and this reversal in trend is attributable to the multidecadal modulations of easterly trade winds over the tropical Pacific [e.g., Merrifield, 2011; Qiu and Chen, 2012; Chen and Wu, 2012].

[38] The influence of oceanic pathway around the Philippine Archipelago is better illustrated by the difference of the Y_b time series between these two runs (Experiment 0 minus Experiment 4, Figure 10a). The Y_b difference, with a standard deviation of 0.25° , is anticorrelated with the Y_b time series in Experiment 4. The negative correlation of -0.61 reconfirms that opening of the Luzon Strait–Sibutu Passage pathway works to reduce the Y_b amplitude. It is important to note that in Figure 10a there exists a conspicuous shift in the multidecadal trend of Y_b difference in the early 1990s. This trend is opposite to that in Figure 9a, reflecting the weaker multidecadal Y_b variability in Experiment 0 than in Experiment 4.

4.2. Kuroshio and Mindanao Current Transports

[39] In this subsection, we further examine the low-frequency variability of KT across 18°N and MCT across 8°N based on the model simulations. The oceanic pathway around the Philippine Archipelago increases the mean KT from 17.9 Sv in Experiment 4 to 24.2 Sv in Experiment 0. This increase of 6.3 Sv is the same as the LST in Experiment 0. The KT time series in these two runs are highly correlated at 0.85 and both contain prominent interannual-to-decadal signals (Figure 9b). The low-frequency KT amplitude in Experiment 0 (2.4 Sv) is lower than that in Experiment 4 (3.0 Sv). In concurrence with the multidecadal changes of Y_b , the KT time series show decreasing trends prior to 1990s and increasing trends thereafter.

Despite the high correlation between these two time series, their difference (Experiment 0 minus Experiment 4, see Figure 10b) shows a trend opposite to that in Figure 9b, indicating the weakening of multidecadal KT variability as a result of the opening of the Sibutu Passage. In

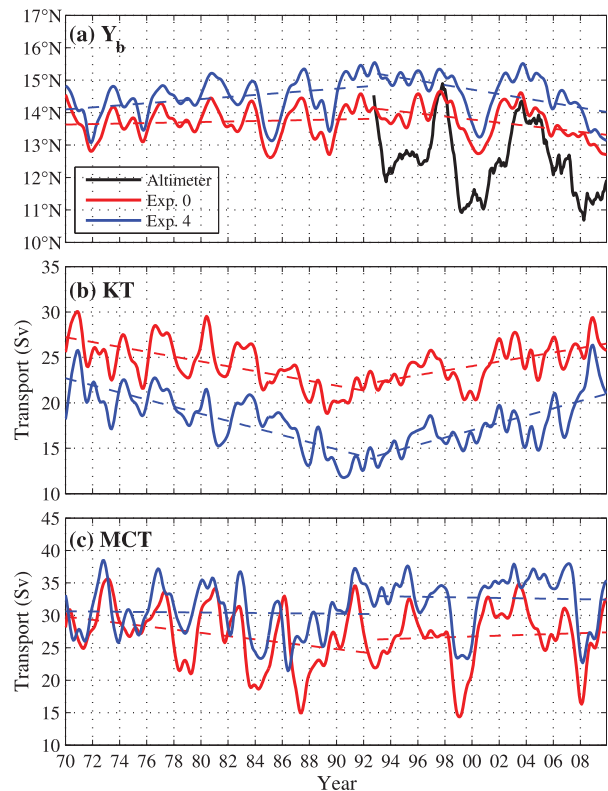


Figure 9. The time series of (a) Y_b , (b) KT, and (c) MCT derived from reduced-gravity model Experiment 0 (red line) and Experiment 4 (blue line). The Y_b time series derived from satellite altimeter observation are also shown in Figure 9a.

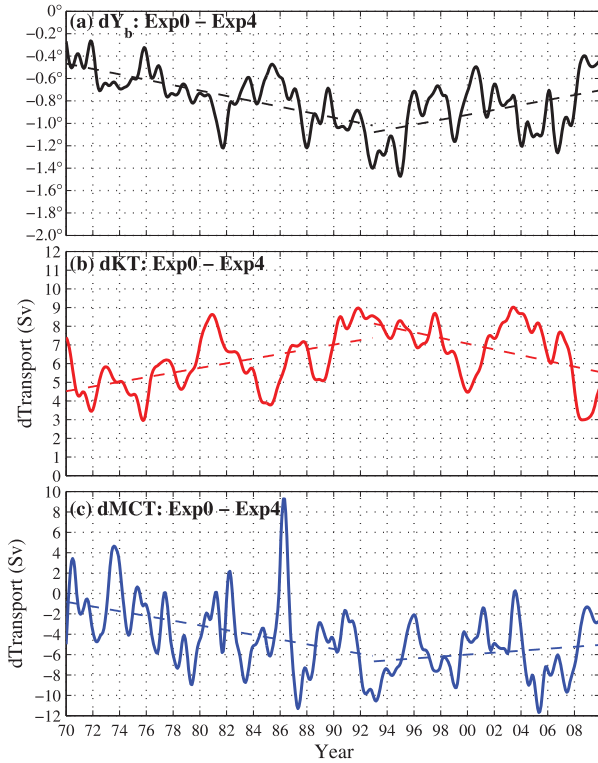


Figure 10. The time series of (a) Y_b difference, (b) KT difference, and (c) MCT difference, between Experiments 0 and 4.

Experiment 4, the KT decreases by 9.0 Sv from 1970 to 1992 and increases by 6.8 Sv from 1993 to 2009. Relative to the values in Experiment 4, the KT changes in Experiment 0 reduces by 2.9 Sv, $\sim 32\%$, during 1970–1992 and increases by 2.6 Sv, $\sim 38\%$, during 1993–2009.

[40] The time-mean southward MCT, on the other hand, decreases from 31.4 Sv in Experiment 4 to 26.9 Sv in Experiment 0. The MCT difference of 4.5 Sv at the 8°N transect is smaller than the LST in Experiment 0, due to the complexity of the anomalous flow pattern to the southeast of the Mindanao Island (Figure 8). To the north of 9.5°N , the MCT difference is nearly the same as the LST. A similar circulation pattern is also simulated by Metzger and Hurlbert [1996]. Due to the strong nonlinearity of the Mindanao Current and its recirculation [Masumoto and Yamagata, 1991; Qiu and Lukas, 1996], a relatively low correlation of 0.69 exists between the MCT in Experiments 0 and 4 (Figure 9c). Associated with the nonlinear flow interactions, the MCT time series display larger low-frequency variability than the KT and this variability is stronger in Experiment 0 (4.7 Sv) than in Experiment 4 (4.1 Sv). In comparison, the multidecadal trends in MCT are not so pronounced as those in Y_b and KT. The trends in Experiment 4 are weak over both the 1970–1992 and 1993–2009 periods (Figure 9c). Opening the oceanic pathway west of the Philippine Archipelago significantly enhances the decreasing trend of MCT from $-0.2\text{ Sv (23 yr)}^{-1}$ ($\sim -0.01\text{ Sv/yr}$) to $-5.7\text{ Sv (23 yr)}^{-1}$ ($\sim -0.25\text{ Sv/yr}$) over the 1970–1992 period. For the 1993–2009 period, the linear trend varies by a smaller amplitude from $-0.5\text{ Sv (17 yr)}^{-1}$ ($\sim -0.03\text{ Sv/yr}$) to $1.1\text{ Sv (17 yr)}^{-1}$ ($\sim 0.06\text{ Sv/yr}$). Based on the satellite altimeter data, Qiu and Chen

[2012] found that over the 1993–2009 period, the portion of the NEC transport circulating into the northward Kuroshio increased much more significantly than the portion into the southward Mindanao Current, in accordance with the model results presented in Figure 9.

[41] It is worth noting that the Luzon Strait and Sibutu Passage transport at 6.3 Sv in Experiment 0 is high compared with the previous observations [e.g., Qu *et al.*, 2000; Liang *et al.*, 2003]. As such, the impact of the Luzon Strait-Sibutu Passage pathway on Y_b , KT, and MT might be overestimated in Figure 10. When the Sibutu Passage transport is reduced to 3.2 Sv in Experiment 6, the Y_b and KT differences of Experiment 6 minus Experiment 7 (not shown) exhibit similar characters of variations as shown in Figures 10a and 10b, but with weaker amplitudes. As the Sibutu Passage transport contains most of the interannual-to-decadal signals of the SCSTF, the decrease of its standard deviation (by $\sim 9\%$) from Experiments 0 to 6 is much smaller than the reduction of its mean value (by $\sim 50\%$). Therefore, the resultant Y_b and KT differences of Experiment 6 minus Experiment 7 decrease only by 25% and 17% in their amplitudes, respectively. The MCT difference of Experiment 6 minus Experiment 7 (not shown) is little correlated with the time series in Figure 10c, implying a significant influence of nonlinearity.

4.3. Dynamical Explanations

[42] Several studies have shown that the strength and variability of SCSTF can be largely explained by Godfrey's [1989] island rule circulating the western flank of the Philippine Archipelago and the eastern Pacific coast [Qu *et al.*, 2000; Wang *et al.*, 2006a, 2006c]. In all these studies, the wind-driven Sverdrup circulation was assumed to be established instantaneously. To better understand the low-frequency circulation changes due to the connectivity of the Philippine Archipelago (Figure 10), we contrast in this subsection two dynamical frameworks: one is the original time-independent island rule proposed by Godfrey [1989] and the other is the time-dependent island rule (TDIR) put forth by Firing *et al.* [1999]. Detailed derivations of these two theories can be found in Appendix A.

[43] As the Godfrey's island rule is derived under the assumption of the steady Sverdrup theory, the total meridional transport (T_0) east of the Philippine coast comprises two components: an interior Sverdrup flow and a WBC:

$$T_0(t) = T_{sv}(y, t) + T_{bc}(y, t) \quad (3)$$

[44] Based on the steady Sverdrup theory, the meridional Sverdrup transport in the interior ocean can be estimated by the zonally integrated WSC:

$$T_{sv}(y, t) = \frac{1}{\rho\beta} \int_{x_e(y)}^{x_w+(y)} \nabla \times \tau(x, y, t) dx \quad (4)$$

[45] With the closure of the pathway around the Philippine Archipelago, the Sverdrup theory and mass balance require that the $T_{bc}(y, t)$ east of the Philippine coast be equal to $-T_{sv}(y, t)$. In this case, Y_b is located at the latitude where $T_{sv}(y, t) = 0$.

[46] When the oceanic pathway west of the Philippine Archipelago is opened, the net meridional transport (T_0)

across the Pacific basin regulates the WBC to $T_{bc}(y, t) = T_0(t) - T_{sv}(y, t)$. Y_b in this case shifts to where $T_0(t) = T_{sv}(y, t)$. The mean T_0 calculated from the ORA-S3 wind forcing is 12.9 Sv, similar to the value of 12.4 Sv in Wang *et al.* [2006a]. This value is greatly reduced by frictional effects within the marginal seas [Qu *et al.*, 2000]. By assuming the frictional effect be the Stommel or Munk-type [Wajsowicz, 1993], one can use the frictionless time series derived from equation (A1) as an index for T_0 governed by the Godfrey's island rule [Wang *et al.*, 2006c]. The differences of Y_b , KT, and MCT between the island rule and the Sverdrup solutions can help us evaluate the extent to which the time-independent dynamics explains the effects of the oceanic pathway around the Philippine Archipelago as shown in Figure 10.

[47] The linear Rossby wave model allows for adjustment processes in the interior ocean associated with the wind-forced baroclinic Rossby waves. It is valid in the absence of the oceanic pathway west of the Philippine Archipelago. As detailed in Appendix A, the TDIR explicitly considers the linear Rossby wave dynamics in the presence of an island. Combining the Rossby wave model and TDIR allows us to quantify the time-dependent dynamical processes associated with the circulation changes around the Philippine Archipelago. In calculating the Sverdrup, island rule, Rossby wave model, and TDIR solutions below, we use the monthly ECMWF-ORAS3 wind stress data and keep the land-ocean geometry the same as the 1.5-layer reduced-gravity model.

[48] Figures 11a–11c compare the differences of Y_b , KT, and MCT derived from Experiment 0 minus Experiment 4, the island rule minus Sverdrup solutions, and the TDIR minus Rossby wave model solutions, respectively. For brevity, we name the results from the island rule minus Sverdrup solutions as the time-independent solutions, and the TDIR minus Rossby wave model solutions as the time-dependent solutions. As all solutions are obtained with the frictionless assumption, the results show larger amplitudes than those of the 1.5-layer reduced-gravity model. In Figure 11, all time series have been normalized to better illustrate their correspondences. It is clear from Figures 11 that the differences of Y_b , KT, and MCT between Experiments 0 and 4 cannot be adequately explained by the time-independent solutions. Their correlation coefficients are 0.05 for the Y_b differences, 0.55 for the KT differences, and 0.20 for the MCT differences.

[49] When the baroclinic Rossby wave adjustment effect in the interior Pacific is considered, the time-dependent solutions better capture the impacts due to the connectivity around the Philippine Archipelago. The correlations between the time-dependent solutions and 1.5-layer model are significantly improved to 0.60 and 0.83 for the Y_b and KT differences, respectively. As shown in Figure 11c, however, the time-dependent solution is still unsuccessful in reproducing the MCT difference between Experiments 0 and 4, with a correlation coefficient of 0.30. The large discrepancy between the MCT time series is likely due to the strong nonlinearity of the Mindanao Current [Masumoto and Yamagata, 1991; Qiu and Lukas, 1996] or its interaction with the other near-equator current systems (e.g., the Halmahera Eddy and the North Equatorial Countercurrent). Notice that the nonlinearity appears to have minor impact

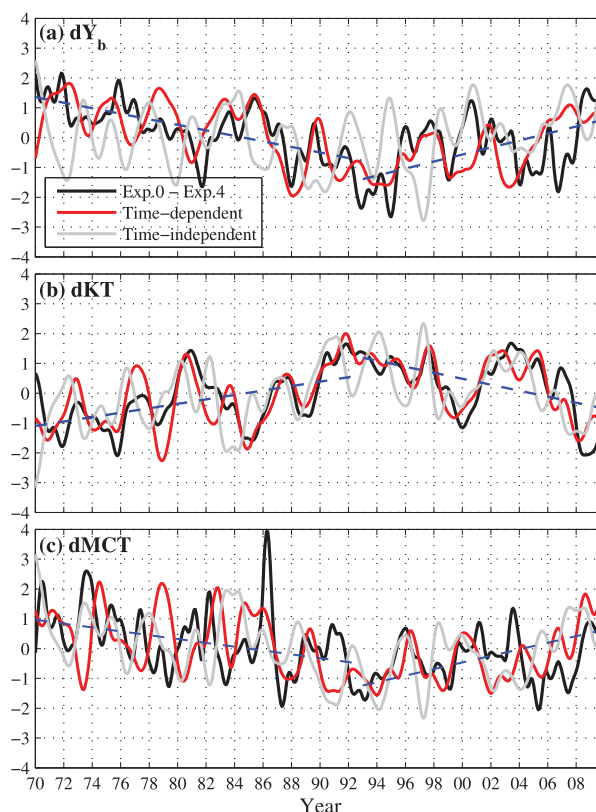


Figure 11. The Normalized (a) Y_b differences, (b) KT differences, and (c) MCT differences derived from the Experiment 0 minus Experiment 4 (black lines), the time-dependent solutions (red lines) and the time-independent solutions (gray lines). The blue lines indicate the trends from the time-dependent solutions.

on the multidecadal MCT modulations associated with the around-island oceanic pathway. From comparing Figures 10 and 11, it is also clear that the time-dependent solutions favorably reproduce the shifts in multidecadal trends of the Y_b , KT, and MCT differences at the early 1990s.

[50] The above comparisons confirm that the oceanic pathway west of the Philippine Archipelago regulates the low-frequency circulation changes in the tropical western North Pacific. Compared to the time-independent solutions, it is the time-dependent island rule incorporating the wind-forced baroclinic adjustment processes that provides the relevant governing dynamics.

5. Summary

[51] Using the multisatellite altimeter observations and a 1.5-layer reduced-gravity model, this study investigated the low-frequency sea level and circulation changes associated with the oceanic connectivity around the Philippine Archipelago. The data-model comparisons demonstrate that the model, though simple in its dynamic formulation, contains the essential physics of the upper ocean wind-driven variability in the western Pacific and the adjacent marginal seas. Both the observations and model simulations reveal that the SSHs to the east and west of the Philippine Archipelago show coherent variations that are closely connected with the ENSO events.

[52] To elucidate the underlying dynamic processes, we designed several sensitivity experiments and attempted to identify the key dynamic components relating to the atmospheric forcing and geometry. The numerical experiments retaining the low-frequency wind signals over different geographical segments (Experiments 1–3) suggest that the winds over the North Pacific tropical gyre are the primary forcing of the SSH changes around the Philippine Archipelago, while winds over the marginal seas and the North Pacific subtropical gyre have only minor influences. After reaching the eastern Philippine coast, the wind-driven baroclinic Rossby waves excite coastal Kelvin waves that propagate clockwise along the Philippine coast into the Sulu Sea and the ESCS at the phase speed of ~ 2.3 m/s. Model experiments which open or close various straits verify that the Sibutu Passage is the key pathway for transmitting the low-frequency SSH signals into the marginal seas in the form of coastal Kelvin waves. Closure of the Luzon Strait, the Karimata Strait and the ITF passages does not significantly affect the low-frequency sea level changes in the Sulu Sea and the ESCS.

[53] Sensitivity model experiments also indicate that the Luzon Strait-Sibutu Passage pathway can modulate the low-frequency variations of the WBC system in the tropical North Pacific. The difference of open minus closed Sibutu Passage (Experiment 0 minus Experiment 4) shows the weakening of Y_b and KT amplitudes due to the existence of oceanic connectivity around the Philippine Archipelago. With the opening of the Sibutu Passage, the reversal in the multidecadal Y_b and KT trends in the early 1990s becomes weaker, implying the oceanic pathway plays a buffer role. In contrast to the Y_b and KT time series, the low-frequency MCT signals show larger amplitudes when the Sibutu Passage is open, probably owing to its strong nonlinearity.

[54] The dynamical processes impacting Y_b , KT, and MCT due to the opened oceanic pathway can be described as follow: the wind-driven downwelling (upwelling) Rossby waves propagate westward to the western boundary of the tropical North Pacific and transmit as coastal Kelvin waves into the ESCS. The rise (decline) of SSH in the western Pacific results in a southward (northward) migration of Y_b and an increase (decrease) of KT. The rise (decline) of SSH to the northwest of the Luzon Island also reduces (enhances) the LST and the Sibutu Passage transport. The changes of the Sibutu Passage transport will feedback to the western Pacific WBC as an anomalous southward (northward) flow to the east of Philippine coast, reducing the southward (northward) Y_b migration and the amplitude of KT enhancement (reduction).

[55] Two linear dynamic frameworks, the Godfrey's island rule and TDIR, are adopted in this study to quantify the changes induced by the opening of the oceanic pathway around the Philippine Archipelago. The TDIR combines the effects of an island and Rossby wave adjustment processes and is capable of explaining the phase changes of Y_b and KT associated with the pathway west of the Philippine Archipelago. In contrast, the Godfrey's island rule fails to capture the detailed phases of the variability. These results indicate the importance of the wind-forced baroclinic Rossby wave adjustment processes to the variability of the WBC system in the tropical North Pacific. The interannual MCT variability cannot be reproduced by either the time-

dependent or time-independent island rule solutions due to the strong nonlinearity of the Mindanao Current.

[56] Throughout this study, we have focused on the wind-driven regional sea level and circulation changes. In addition to the wind forcing, effects of thermohaline processes and mesoscale eddy activities can also be crucial for the western Pacific Ocean circulation, especially in the region north of 18°N [Kobashi and Kubokawa, 2012; Chang and Oey, 2012; Qiu and Chen, 2013] where the performance of 1.5-layer reduced-gravity model becomes less effective. Meanwhile, sea level and circulation changes in the western SCS are also not adequately simulated by our model, probably due to the lack of realistic bottom topography and stratification in the model. It will be important for future studies to utilize the synergy of in situ observations and high-resolution three-dimensional models to quantify these effects in comparison with the wind forcings.

Appendix A: Time-Dependent Island Rule

[57] According to Godfrey's [1989] island rule, mass conservation requires that the meridional transport across individual zonal sections between the island and the ocean's eastern boundary be constant in the steady state. This constant transport T_0 is determined by the surface wind stress along the path that circulates the western coast of the island, the eastern boundary of the ocean basin, and along the latitudes of the island's northern and southern tips, that is,

$$T_0 = \frac{\oint_{ABCD} \tau^{(l)} dl}{\rho(f_D - f_A)} \quad (\text{A1})$$

where $\tau^{(l)}$ is the tangential wind stress along the path, A is at the southern tip of Mindanao, D is at the northern tip of Luzon. B and C denote the two points at the same latitudes as A and D near the American coast (see Figure A1), and f_A and f_D are the Coriolis parameters at A and D , respectively.

[58] The island rule is steady and assumes the oceanic adjustment is achieved instantaneously. Firing *et al.* [1999] extend Godfrey's island rule to the upper-layer flow in the baroclinic time-dependent case. In this study, we simplify the TDIR put forth by Firing *et al.* [1999] to the linear, 1.5-layer reduced-gravity model:

$$f\mathbf{k} \times \mathbf{u} = -g'\nabla h + \frac{\tau}{\rho_0 H} + F_r(\mathbf{u}) \quad (\text{A2})$$

$$\frac{\partial h}{\partial t} + H\nabla \cdot \mathbf{u} = 0 \quad (\text{A3})$$

where $F_r(\mathbf{u})$ represents the horizontal momentum dissipation due to interfacial friction or lateral eddy mixing, which is important only within the boundary layer east of the island, h is the time-varying upper layer thickness, and H is the time-mean upper layer thickness. Neglecting the $\partial \mathbf{u} / \partial t$ term in equation (A2) is equivalent to the adoption of the long-wave approximation.

[59] Combining equations (A2) and (A3) leads to the following linear vorticity equation:

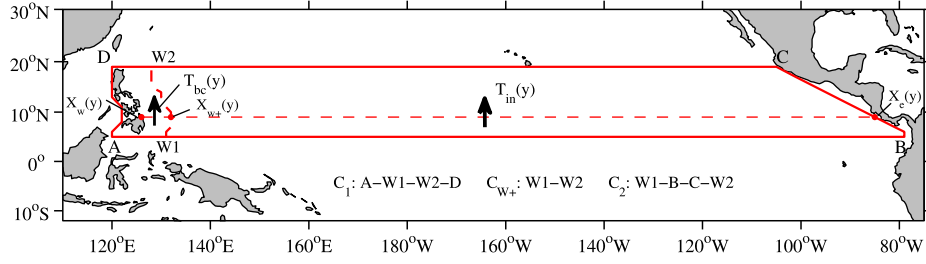


Figure A1. Schematic showing the integration paths for the TDIR: $x_w(y)$ and $x_e(y)$ are the longitudes of the island's west coast and the oceanic eastern boundary at latitude y , and $x_{w+}(y)$ is the offshore edge of the island's western boundary layer. $T_{bc}(y)$ represents the meridional transport of the western boundary current. $T_{in}(y)$ is the interior meridional transport between $x_{w+}(y)$ and $x_e(y)$. For easy viewing, the zonal extension of western boundary layer is amplified from 2° to 6° .

$$\frac{\partial h}{\partial t} + c_R \frac{\partial h}{\partial x} = -\frac{1}{\rho_0} \nabla \times \left(\frac{\tau}{f} \right) \equiv B(x, y, t) \quad (\text{A4})$$

where $c_R = -\beta g' H / f^2$ is the baroclinic long Rossby wave speed. Integrating equation (A4) westward from the eastern boundary (x_e) yields the solution:

$$h(x, y, t) = h\left(x_e, y, t - \frac{x - x_e}{c_R}\right) + \frac{1}{c_R} \int_{x_e}^x B\left(x', y, t - \frac{x - x'}{c_R}\right) dx' \quad (\text{A5})$$

[60] Across a fixed latitude y east of the island, the interior meridional transport is:

$$T_{in}(y, t) \equiv \int_{x_{w+}}^{x_e(y)} H v dx \quad (\text{A6})$$

where $x_e(y)$ is the ocean's eastern boundary at the latitude y , and $x_{w+}(y)$ is the x position just offshore of the WBC (see Figure A1). Using equations (A2) and (A5), $T_{in}(y, t)$ can be expressed by:

$$\begin{aligned} T_{in}(y, t) &= \int_{x_e}^{x_{w+}} \left(\frac{\tau^x}{\rho_0 f} - \frac{g' H}{f} \frac{\partial h}{\partial x'} \right) dx' \\ &= \int_{x_e}^{x_{w+}} \frac{\tau^x}{\rho_0 f} dx' - \frac{g' H}{f c_R} \int_{x_e}^{x_{w+}} B\left(x', y, t - \frac{x_{w+} - x'}{c_R}\right) dx' \end{aligned} \quad (\text{A7})$$

[61] The first term on the right-hand side of equation (A7) is the meridional component of the Ekman transport; the second term is the geostrophic transport associated with the baroclinic response to the wind-driven Ekman Pumping. Here the wave signals radiated from the eastern boundary is ignored because its influence is minor in the interior ocean a few Rossby radii away from the eastern coast [Fu and Qiu, 2002]. Equation (A7) extends the steady Sverdrup balance to the time-dependent Sverdrup balance including the local Ekman component and the baroclinic response due to Rossby wave propagation.

[62] Now consider the meridional transport within the western boundary layer east of the island:

$$T_{bc}(y, t) \equiv \int_{x_w(y)}^{x_{w+}(y)} H v dx \quad (\text{A8})$$

[63] Using the mass balance inside the boundary layer and ignoring the local divergence in h inside the boundary layer, we have:

$$T_{bc}(y_n, t) - T_{bc}(y_s, t) + \int_{C_{w+}} H \mathbf{k} \times \mathbf{u} \cdot d\mathbf{l} = 0 \quad (\text{A9})$$

where C_{w+} is the segment of C_1 that runs along the offshore edge of the WBC from the northern tip to the southern tip of the island (Figure A1).

[64] To determine $T_{bc}(y_n, t)$, we follow Godfrey's [1989] island rule:

$$\oint_{C_1} f \mathbf{k} \times \mathbf{u} \cdot d\mathbf{l} = \oint_{C_1} \frac{\tau(t) \cdot d\mathbf{l}}{\rho_0 H} \quad (\text{A10})$$

[65] On the β -plane approximation, the above equation becomes:

$$\beta \oint_{C_1} y \mathbf{k} \times \mathbf{u} \cdot d\mathbf{l} = \oint_{C_1} \frac{\tau(t) \cdot d\mathbf{l}}{\rho_0 H} \quad (\text{A11})$$

or

$$y_n T_{bc}(y_n, t) - y_s T_{bc}(y_s, t) + \int_{C_{w+}} y H \mathbf{k} \times \mathbf{u} \cdot d\mathbf{l} = \oint_{C_1} \frac{\tau(t) \cdot d\mathbf{l}}{\rho_0 \beta} \quad (\text{A12})$$

[66] Eliminating $T_{bc}(y_s, t)$ from equations (A9) to (A12), we have:

$$T_{bc}(y_n, t) = \frac{1}{\Delta y} \oint_{C_1} \frac{\tau(t) \cdot d\mathbf{l}}{\rho_0 \beta} - \frac{1}{\Delta y} \int_{C_{w+}} (y - y_s) H \mathbf{k} \times \mathbf{u} \cdot d\mathbf{l} \quad (\text{A13})$$

where $\Delta y = y_n - y_s$. To evaluate the last term in equation (A13), we use the mass conservation equation (A3) and integrate it from x_{w+} to x_e :

$$\begin{aligned} \int_{x_{w+}}^{x_e} \frac{\partial h}{\partial t} dx &= -H \int_{x_{w+}}^{x_e} \frac{\partial u}{\partial x} dx - H \int_{x_{w+}}^{x_e} \frac{\partial v}{\partial y} dx \\ &= H u(x_{w+}) - \frac{\partial}{\partial y} T_{in}(y, t) - H v(x_{w+}) \frac{dx_{w+}}{dy} \end{aligned} \quad (\text{A14})$$

[67] The last term in equation (A14) above comes from the following Leibniz rule:

$$\frac{\partial}{\partial y} \int_{x_{w+}}^{x_e} v dx = \int_{x_{w+}}^{x_e} \frac{\partial v}{\partial y} dx + v(x_e) \frac{dx_e}{dy} - v(x_{w+}) \frac{dx_{w+}}{dy} \quad (\text{A15})$$

[68] Multiplying equation (A14) by $(y - y_s)$, integrating in y , and substituting in equation (A13), we have:

$$\begin{aligned} T_{bc}(y_n, t) &= \frac{1}{\Delta y} \oint_{C_1} \frac{\tau(t) \cdot d\mathbf{l}}{\rho_0 \beta} - \frac{1}{\Delta y} \int_{y_s}^{y_n} \int_{x_{w+}}^{x_e} (y - y_s) \frac{\partial h}{\partial t} dx dy \\ &\quad - \frac{1}{\Delta y} \int_{y_s}^{y_n} (y - y_s) \frac{\partial}{\partial t} T_{in}(y, t) dy \\ &= \frac{1}{\Delta y} \oint_{C_1} \frac{\tau(t) \cdot d\mathbf{l}}{\rho_0 \beta} - \frac{1}{\Delta y} \int_{y_s}^{y_n} \int_{x_{w+}}^{x_e} (y - y_s) \frac{\partial h}{\partial t} dx dy \\ &\quad - T_{in}(y_n, t) + \frac{1}{\Delta y} \int_{y_s}^{y_n} T_{in}(y, t) dy \end{aligned} \quad (\text{A16})$$

[69] Equation (A16) provides the expression of the meridional transport within the western boundary at the northern tip off the island. The first term on the right-hand side is the local wind forcing around the island. The second term depends on the rate of change of averaged upper-layer thickness and is called the “storage” term by *Firing et al.* [1999]. The third and fourth terms are the meridionally averaged interior meridional transport minus the local interior meridional transport along y_n .

[70] After obtaining the transport of the WBC at y_n , it is straightforward to derive the boundary current transport at any other latitude y by using the mass conservation equation (A3) inside the box between y and y_n east of the island:

$$T_{bc}(y, t) = T_{bc}(y_n, t) + T_{in}(y_n, t) - T_{in}(y, t) + \int_y^{y_n} \int_{x_{w+}}^{x_e} \frac{\partial h}{\partial t} dx dy \quad (\text{A17})$$

[71] Utilizing the time-varying surface wind forcing and following equations (A5), (A7), and (A16), the $T_{bc}(y, t)$ in equation (A17) can be numerically calculated. By definition, the NEC bifurcation occurs at $y = Y_b$ where $T_{bc}(y_b, t) = 0$.

[72] On the other hand, in a closed basin without island, the upper layer thickness (h) in the linear Rossby wave model is also determined by equation (A5). Following *Qiu and Lukas* [1996], mass conservation requires the NEC to bifurcate at the latitude where $h = 0$ if the detailed WBC structures are neglected. So Y_b in the Rossby wave model is defined as where the mean h within the 2° band off the western boundary is zero. Because $T_{bc}(y_b, t) = 0$, the WBC transport at other latitudes can be expressed according to the mass balance as:

$$T_{bc}(y, t) = \int_y^{y_b} \int_{x_{w+}}^{x_e} \frac{\partial h}{\partial t} dx dy - T_{in}(y, t) + T_{in}(y_b, t). \quad (\text{A18})$$

[73] **Acknowledgments.** We thank Shuiming Chen for many helpful discussions. Comments from reviewers are highly appreciated. The merged satellite altimeter data were provided by the CLS Space Oceanography Division. The ECMWF ORA-S3 data were provided by the Asia-Pacific Data Research Center, University of Hawaii. W.Z. and Y.D. are supported by Strategic Priority Research Program of the Chinese Academy of Sciences (XDA11010103), National Basic Research Program of China (2011CB403503), National Natural Science Foundation of China

(41176028, 41176024), and CAS project (SQ200809). B.Q. is supported by NSF through grant OCE-0926594.

References

- Chang, Y.-L., and L.-Y. Oey (2012), The Philippines-Taiwan Oscillation: Monsoon-like interannual oscillation of the subtropical-tropical western North Pacific wind system and its impact on the ocean, *J. Clim.*, **25**, 1597–1618.
- Chelton, D. B., R. A. de Szoeke, M. G. Schlax, K. E. Naggar, and N. Siwertz (1998), Geographical variability of the first baroclinic Rossby radius of deformation, *J. Phys. Oceanogr.*, **28**, 433–460.
- Chen, Z., and L. Wu (2011), Dynamics of the seasonal variation of the North Equatorial Current bifurcation, *J. Geophys. Res.*, **116**, C02018, doi:10.1029/2010JC006664.
- Chen, Z., and L. Wu (2012), Long-term change of the Pacific North Equatorial Current bifurcation in SODA, *J. Geophys. Res.*, **117**, C06016, doi:10.1029/2011JC007814.
- Chu, P. C., and R. Li (2000), South China Sea isopycnal-surface circulation, *J. Phys. Oceanogr.*, **30**, 2419–2438, doi:10.1175/1520-0485(2000)030<2419:SCSISC>2.0.CO;2.
- Cushman-Roisin, B. (1984), On the maintenance of the Subtropical Front and its associated countercurrent, *J. Phys. Oceanogr.*, **14**, 1179–1190.
- Du, Y., and T. Qu (2010), Three inflow pathways of the Indonesian throughflow as seen from the simple ocean data assimilation, *Dyn. Atmos. Oceans*, **50**, 233–256, doi:10.1016/j.dynatmoce.2010.04.001.
- Ducet, N., P.-Y. Le Traon, and G. Reverdin (2000), Global high-resolution mapping of ocean circulation from TOPEX/Poseidon and ERS-1 and -2, *J. Geophys. Res.*, **105**, 19,477–19,498.
- Durland, T. S., and B. Qiu (2003), Transmission of subinertial Kelvin waves through a strait, *J. Phys. Oceanogr.*, **33**, 1337–1350.
- Fang, G., H. Chen, Z. Wei, Y. Wang, X. Wang, and C. Li (2006), Trends and interannual variability of the South China Sea surface winds, surface height, and surface temperature in the recent decade, *J. Geophys. Res.*, **111**, C11S16, doi:10.1029/2005JC003276.
- Fang, G., Y. Wang, Z. Wei, Y. Fang, F. Qiao, and X. Hu (2009), Inter-ocean circulation and heat and freshwater budgets of the South China Sea based on a numerical model, *Dyn. Atmos. Oceans*, **47**, 55–72, doi:10.1016/j.dynatmoce.2008.09.003.
- Feng, M., Y. Li, and G. Meyers (2004), Multidecadal variations of Fremantle sea level: Footprint of climate variability in the tropical Pacific, *Geophys. Res. Lett.*, **31**, L16302, doi:10.1029/2004GL019947.
- Fine, R. A., R. Lukas, F. M. Bingham, M. J. Warner, and R. H. Gammon (1994), The western equatorial Pacific: A water mass crossroads, *J. Geophys. Res.*, **99**, 25,063–25,080, doi:10.1029/94JC02277.
- Firing, E., B. Qiu, and W. Miao (1999), Time-dependent island rule and its application to the time-varying north Hawaiian ridge current, *J. Phys. Oceanogr.*, **29**, 2671–2688.
- Fu, L.-L., and B. Qiu (2002), Low-frequency variability of the North Pacific Ocean: The roles of boundary- and wind-driven baroclinic Rossby waves, *J. Geophys. Res.*, **107**(C12), 3220, doi:10.1029/2001JC001131.
- Godfrey, J. S. (1989), A Sverdrup model of the depth-integrated flow for the world ocean allowing for island circulations, *Geophys. Astrophys. Fluid Dyn.*, **45**, 89–112.
- Gordon, A. L., J. Sprintall, and A. Ffield (2011), Regional oceanography of the Philippine Archipelago, *Oceanography*, **24**(1), 14–27, doi:10.5670/oceanog.2011.01.
- Gordon, A. L., B. A. Huber, E. J. Metzger, R. D. Susanto, H. E. Hurlburt, and T. R. Adi (2012), South China Sea throughflow impact on the Indonesian throughflow, *Geophys. Res. Lett.*, **39**, L11602, doi:10.1029/2012GL052021.
- Han, W., A. M. Moore, E. Di Lorenzo, A. L. Gordon, and J. Lin (2009), Seasonal surface ocean circulation and dynamics in the Philippine archipelago region during 2004–2008, *Dyn. Atmos. Oceans*, **47**, 114–137.
- Hu, D., and M. Cui (1991), The western boundary current of the Pacific and its role in the climate, *Chin. J. Oceanol. Limnol.*, **9**, 1–14, doi:10.1007/BF02849784.
- Johnson, H. L., and C. Garrett (2006), What fraction of a Kelvin wave incident on a narrow strait is transmitted?, *J. Phys. Oceanogr.*, **36**, 945–954.
- Kobashi, F., and A. Kubokawa (2012), Review on North Pacific subtropical countercurrents and subtropical fronts: Role of mode waters in ocean circulation and climate, *J. Oceanogr.*, **68**, 21–43.
- Kobashi, F., H. Mitsudera, and S. P. Xie (2006), Three subtropical fronts in the North Pacific: Observational evidence for mode water-induced

- subsurface frontogenesis, *J. Geophys. Res.*, **111**, C09033, doi:10.1029/2006JC003479.
- Kubokawa, A. (1997), A two-level model of subtropical gyre and subtropical countercurrent, *J. Oceanogr.*, **53**, 231–244.
- Liang, W.-D., T. Y. Tang, Y. J. Yang, M. T. Ko, and W.-S. Chuang (2003), Upper-ocean currents around Taiwan, *Deep Sea Res., Part II*, **50**, 1085–1105, doi:10.1016/S0967-0645(03)00011-0.
- Liu, Q., M. Feng, and D. Wang (2011), ENSO-induced interannual variability in the southeastern South China Sea, *J. Oceanogr.*, **67**, 127–133, doi:10.1007/s10872-011-0002-y.
- Lukas, R., T. Yamagata, and J. P. McCreary (1996), Pacific low-latitude western boundary currents and the Indonesian throughflow, *J. Geophys. Res.*, **101**, 12,209–12,216, doi:10.1029/96JC01204.
- Masumoto, Y., and T. Yamagata (1991), Response of the western tropical Pacific to the Asian winter monsoon: The generation of the Mindanao Dome, *J. Phys. Oceanogr.*, **21**(9), 1386–1398, doi:10.1175/1520-0485(1991)021<1386:ROTWTP>2.0.CO;2.
- Merrifield, M. A. (2011), A shift in western tropical Pacific sea level trends during the 1990s, *J. Clim.*, **24**, 4126–4138.
- Metzger, E. J. (2003), Upper ocean sensitivity to wind forcing in the South China Sea, *J. Oceanogr.*, **59**, 783–798, doi:10.1023/B:JOCE.0000009570.41358.c5.
- Metzger, E. J., and H. Hurlburt (1996), Coupled dynamics of the South China Sea, the Sulu Sea, and the Pacific Ocean, *J. Geophys. Res.*, **101**, 12,331–12,352.
- Meyers, G. (1996), Variation of Indonesian throughflow and the El Niño–Southern oscillation, *J. Geophys. Res.*, **101**, 12,255–12,263, doi:10.1029/95JC03729.
- Nitani, H. (1972), Beginning of the Kuroshio, in *Kuroshio: Physical Aspects of the Japan Current*, edited by H. Stommel and K. Yashida, pp. 129–163, Univ. of Wash. Press, Seattle.
- Qiu, B. (1999), Seasonal eddy field modulation of the North Pacific Subtropical Countercurrent: TOPEX/Poseidon observations and theory, *J. Phys. Oceanogr.*, **29**, 2471–2486.
- Qiu, B., and S. Chen (2010), Interannual-to-decadal variability in the bifurcation of the North Equatorial Current off the Philippines, *J. Phys. Oceanogr.*, **40**(11), 2525–2538, doi:10.1175/2010JPO4462.1.
- Qiu, B., and S. Chen (2012), Multidecadal sea level and gyre circulation variability in the northwestern tropical Pacific Ocean, *J. Phys. Oceanogr.*, **42**(1), 193–206, doi:10.1175/JPO-D-11-061.1.
- Qiu, B., and S. Chen (2013), Concurrent decadal mesoscale eddy modulations in the western North Pacific subtropical gyre, *J. Phys. Oceanogr.*, **43**(2), 344–358, doi:10.1175/JPO-D-12-0133.1.
- Qiu, B., and R. Lukas (1996), Seasonal and interannual variability of the North Equatorial Current, the Mindanao Current, and the Kuroshio along the Pacific western boundary, *J. Geophys. Res.*, **101**, 12,315–12,330, doi:10.1029/95JC03204.
- Qu, T., and R. Lukas (2003), The bifurcation of the North Equatorial Current in the Pacific, *J. Phys. Oceanogr.*, **33**(1), 5–18, doi:10.1175/1520-0485(2003)033<0005:TBOTNE>2.0.CO;2.
- Qu, T., and Y. T. Song (2009), Mindoro Strait and Sibutu Passage transports estimated from satellite data, *Geophys. Res. Lett.*, **36**, L09601, doi:10.1029/2009GL037314.
- Qu, T., H. Mitsudera, and T. Yamagata (2000), Intrusions of the North Pacific Waters into the South China Sea, *J. Geophys. Res.*, **105**, 6415–6424, doi:10.1029/1999JC000323.
- Qu, T., Y. Y. Kim, M. Yaremchuk, T. Tozuka, A. Ishida, and T. Yamagata (2004), Can the Luzon Strait transport play a role in conveying the impact of ENSO to the South China Sea?, *J. Clim.*, **17**, 3644–3657, doi:10.1175/1520-0442(2004)017<3644:CLSTPA>2.0.CO;2.
- Qu, T., Y. Du, G. Meyers, A. Ishida, and D. Wang (2005), Connecting the tropical Pacific with Indian Ocean through South China Sea, *Geophys. Res. Lett.*, **32**, L24609, doi:10.1029/2005GL024698.
- Qu, T., Y. Du, and H. Sasaki (2006), South China Sea throughflow: A heat and freshwater conveyor, *Geophys. Res. Lett.*, **33**, L23617, doi:10.1029/2006GL028350.
- Rio, M. H., S. Guinehut, and G. Larnicol (2011), New CNESCLS09 global mean dynamic topography computed from the combination of GRACE data, altimetry, and in situ measurements, *J. Geophys. Res.*, **116**, C07018, doi:10.1029/2010JC006505.
- Sprattall, J., A. L. Gordon, P. Flament, and C. L. Villanoy (2012), Observations of exchange between the South China Sea and the Sulu Sea, *J. Geophys. Res.*, **117**, C05036, doi:10.1029/2011JC007610.
- Tian, J., Q. Yang, X. Liang, L. Xie, D. Hu, F. Wang, and T. Qu (2006), Observation of Luzon Strait transport, *Geophys. Res. Lett.*, **33**, L19607, doi:10.1029/2006GL026272.
- Toole, J. M., R. C. Millard, Z. Wang, and S. Pu (1990), Observations of the Pacific North Equatorial Current bifurcation at the Philippine coast, *J. Phys. Oceanogr.*, **20**(2), 307–318, doi:10.1175/1520-0485(1990)020<0307:OOTPNE>2.0.CO;2.
- Wajswicz, R. C. (1993), The circulation of the depth-integrated flow around an island with application to the Indonesian throughflow, *J. Phys. Oceanogr.*, **23**, 1470–1484.
- Wang, B., R. Wu, and X. Fu (2000), Pacific-East Asia teleconnection: How does ENSO affect East Asian climate?, *J. Clim.*, **13**, 1517–1536.
- Wang, D., Q. Liu, R. X. Huang, Y. Du, and T. Qu (2006a), Interannual variability of the South China Sea throughflow inferred from wind data and an ocean data assimilation product, *Geophys. Res. Lett.*, **33**, L14605, doi:10.1029/2006GL026316.
- Wang, G., D. Chen, and J. Su (2006b), Generation and life cycle of the dipole in the South China Sea summer circulation, *J. Geophys. Res.*, **111**, C06002, doi:10.1029/2005JC003314.
- Wang, Y., G. Fang, Z. Wei, F. Qiao, and H. Chen (2006c), Interannual variation of the South China Sea circulation and its relation to El Niño, as seen from a variable grid global ocean model, *J. Geophys. Res.*, **111**, C11S14, doi:10.1029/2005JC003269.
- Wijffels, S., and G. Meyers (2004), An intersection of oceanic waveguides: Variability in the Indonesian throughflow region, *J. Phys. Oceanogr.*, **34**, 1232–1253.
- Willis, J. K., D. P. Chambers, C.-Y. Kuo, and C. K. Shum (2010), Global sea level rise—Recent progress and challenges for the decade to come, *Oceanography*, **23**, 26–35.
- Wu, C.-R. (2013), Interannual modulation of the Pacific Decadal Oscillation (PDO) on the low-latitude western North Pacific, *Prog. Oceanogr.*, **110**, 49–58.
- Wyrtki, K. (1961), Physical oceanography of the southeast Asian waters: Scientific results of marine investigations of the South China Sea and the Gulf of Thailand 1959–1961, *NAGA Rep. 2*, 195 pp., Scripps Inst. of Oceanogr., La Jolla, Calif.
- Yaremchuk, M., and T. Qu (2004), Seasonal variability of the large-scale currents near the coast of the Philippines, *J. Phys. Oceanogr.*, **34**, 844–855, doi:10.1175/1520-0485(2004)034<0844:SVOTLC>2.0.CO;2.
- Yaremchuk, M., J. McCreary Jr., Z. Yu, and R. Furue (2009), The South China Sea throughflow retrieved from climatological data, *J. Phys. Oceanogr.*, **39**, 753–767, doi:10.1175/2008JPO3955.1.
- Yu, K., and T. Qu (2013), Imprint of the Pacific decadal oscillation on the South China Sea throughflow variability, *J. Clim.*, **26**, 9797–9805, doi:10.1175/JCLI-D-12-00785.1.
- Zheng, Z.-W., C.-R. Ho, and N.-J. Kuo (2007), Mechanism of weakening of west Luzon eddy during La Niña years, *Geophys. Res. Lett.*, **34**, L11604, doi:10.1029/2007GL030058.
- Zhuang, W., S.-P. Xie, D. Wang, B. Taguchi, H. Aiki, and H. Sasaki (2010), Intraseasonal variability in sea surface height over the South China Sea, *J. Geophys. Res.*, **115**, C04010, doi:10.1029/2009JC005647.